Tomography of near-field radiative heat exchange between mesoscopic bodies immersed in a thermal bath

Florian Herz [⬤],[*] Riccardo Messina [⬤], and Philippe Ben-Abdallah

Laboratoire Charles Fabry, UMR 8501, Institut d'Optique, CNRS, *Université Paris-Saclay*, 91127 Palaiseau Cedex, France

A tomographic study of near-field radiative heat exchanges between a mesoscopic object and a substrate immersed in a thermal bath is carried out within the theoretical framework of fluctuational electrodynamics. By using the discrete-dipole-approximation method, we compute the power density distribution for radiative exchanges and highlight the major role played by many-body interactions in these transfers. Additionally, we emphasize the close relationship between power distribution and eigenmodes within the solid paving the way to applications for hot-spot targeting at deep subwavelength scale by shape optimization.

I. INTRODUCTION

Concentrating the heat emitted by a hot object placed at close distance to a base material if of significant relevance for practical uses such as nanophotolithography [1], to engrave patterning nanometer-scale structures on material surfaces, heat-assisted magnetic recording [2,3] for data storage in hard-disk writing technology, or to make local temperature measurements using the near-field scanning thermal microscopy technique [4–8]. Indeed, at distances smaller than the thermal wavelength $\lambda_{\text{th}} = \hbar c / k_B T$ to the source, in which k_B is Boltzmann's constant, the exchanged heat flux can surpass the flux predicted by the famous Stefan-Boltzmann's law (blackbody limit [9]) by several orders of magnitude [10–12] due to the contribution of evanescent photons which are superimposed on the propagative ones. In all these applications, a small section of the solid substrate is heated due to a super-Planckian heat flux to elevate its temperature beyond its melting point or beyond the Curie temperature of magnetic materials to demagnetize them locally. Therefore, to understand the underlying physics which govern the interactions of the electromagnetic field radiated by thermal emitters with microscope tips is of crucial importance. Despite recent progress in modeling these objects [13–19], challenges remain in fully understanding this physics. Among the open questions is the description of many-body mechanisms [20–22] which drive interactions and heat exchanges between mesoscopic objects and the field radiated by surrounding thermal emitters.

In the present work, we investigate this problem in detail within the framework of the fluctuational-electrodynamics theory [23]. We first introduce a theoretical model to analyze the radiative heat exchanges among coupled dipoles, a substrate, and the surrounding environment. We explore how individual resonant modes, potential surface modes, and collective modes contribute to these exchanges. Subsequently, employing the discrete dipole approximation (DDA) method

for thermal emitters [19,24], we compute the distribution of the power density for radiative exchanges within a mesoscopic object immersed in a thermal environment and positioned above a substrate at various distances. Thus, we provide a complete tomographic image of exchanges between each part of the object and its surrounding environment. By examining these power exchanges and the internal power spectra across the different regions within the solid, we reveal the diverse mechanisms driving heat exchanges between a tip and a substrate. Beyond the practical problem of near-field thermal microscopy, we highlight the major role played by N-body effects on the energy exchanges between a mesocopic object and its surrounding environment. Additionally, we highlight the close connection existing between the power distribution within a solid and its eigenmodes thereby paving the way towards shape optimization for hot spot targeting.

The article is structured as follows: In Sec. II we introduce our DDA method which we apply to two coupled dipoles in Sec. III, both in vacuum (Sec. III A) and above a substrate (Sec. III B). Subsequently, in Sec. IV we discuss the tomography of a two-dimensional (2D) disk spatially (Sec. IV A) and spectrally (Sec. IV B). In the spectral analysis we also investigate a ring configuration with and without substrate (Sec. IV B 1), special particles on a ring (Sec. IV B 2), and the spatial distribution for special frequencies (Sec. IV B 3). Sec. V covers the tomography of a 3D geometry that mimics thermal near-field microscopy experiments. In Sec. VI we end up with our conclusion.

II. THEORETICAL FRAMEWORK

The system we consider is made of a collection of N spherical particles of radii R_β ($\beta \in \{1, \dots, N\}$) and positions $\mathbf{r}_\beta$ placed in proximity to a substrate occupying the region $z < 0$. Moreover, the particles are exposed to an environmental field, which can be thought as coming from the external boundaries, placed at large distance $z > 0$ from particles and substrate. In the context of the dipolar approximation, we are going to describe each particle as an electric dipolar moment $\mathbf{p}_\beta$.

---

[*]Contact author: florian.herz@institutoptique.fr

Note that the dipole approximation is valid for radii of each dipole that are much smaller than the thermal wavelength and the edge-to-edge distance between this dipole and the substrate d [25,26]. In practice, the latter condition refers to $2R_\beta \leqslant d$ [27]. Another limiting factor for DDA is that it fails to describe metals in the infrared regime due to the presence of eddy currents [18] and it requires a considerably larger number of elementary dipoles if the material's permittivity is high [28]. From a numerical point of view, DDA becomes also less effective for larger systems for which it is more suitable to use alternative methods like the boundary element method [29].

To calculate the power dissipated into each particle in this configuration, we first need to determine the electric field and the electric dipole moments at each $\mathbf{r}_\beta$. The electric field $\mathbf{E}$ at any position $\mathbf{r}$ can be decomposed into a contribution of the environmental field $\mathbf{E}_{\text{env}}$ and the ones which are induced by dipole moments $\mathbf{p}_\beta$ at the position $\mathbf{r}_\beta$, yielding

$$\mathbf{E}(\mathbf{r}) = \mathbf{E}_{\text{env}}(\mathbf{r}) + \mu_0 \omega^2 \sum_{\beta=1}^{N} \mathbb{G}_E(\mathbf{r}, \mathbf{r}_\beta) \mathbf{p}_\beta. \quad (1)$$

Herein $\mathbb{G}_E(\mathbf{r}, \mathbf{r}_\beta)$ describes the electric Green's function at observation point $\mathbf{r}$ caused by an electric dipole moment at source point $\mathbf{r}_\beta$, ω represents the angular frequency and μ_0 the vacuum permeability. Note that since we only take into account polar materials like silicon carbide (SiC), we can safely neglect the magnetic response of the system as it would be necessary in the case of metals [30–34]. The electric dipole moments $\mathbf{p}_\beta$ can be decomposed into a fluctuating part $\mathbf{p}_{\beta,\text{fl}}$ and an induced one $\mathbf{p}_{\beta,\text{ind}}$, the latter depending on the electric field in Eq. (1) at position $\mathbf{r}_\beta$, so that

$$\mathbf{p}_\beta = \mathbf{p}_{\beta,\text{fl}} + \varepsilon_0 \alpha_\beta \mathbf{E}(\mathbf{r}_\beta)$$

$$= \mathbf{p}_{\beta,\text{fl}} + \varepsilon_0 \alpha_\beta \mathbf{E}_{\text{env}}(\mathbf{r}_\beta) + k_0^2 \alpha_\beta \sum_{\gamma=1}^{N} \mathbb{G}_E(\mathbf{r}_\beta, \mathbf{r}_\gamma) \mathbf{p}_\gamma. \quad (2)$$

In the last expression, ε_0 denotes the vacuum permittivity, $k_0 = \omega/c$ the wave number in vacuum, c the velocity of light in vacuum,

$$\alpha_\beta = \frac{\alpha_{\text{CM},\beta}}{1 - i\frac{k_0^3}{6\pi}\alpha_{\text{CM},\beta}}, \quad (3)$$

$$\alpha_{\text{CM},\beta} = 4\pi R_\beta^3 \frac{\varepsilon_\beta - 1}{\varepsilon_\beta + 2}, \quad (4)$$

the dressed and the Clausius-Mosotti polarizabilities in the weak form of the coupled dipole moments [21,35–38], respectively and ε_β the dielectric permittivity of particle β. In the following, we will use SiC for both particles and substrate. Its dielectric permittivity can be described by a Drude-Lorentz model [39]

$$\varepsilon_\beta(\omega) = \varepsilon_\infty \frac{\omega_{\text{LO}}^2 - \omega^2 - i\omega\Gamma}{\omega_{\text{TO}}^2 - \omega^2 - i\omega\Gamma} \quad (5)$$

with the following parameters: $\varepsilon_\infty = 6.7$, $\omega_{\text{LO}} = 1.827 \times 10^{14}$ rad/s, $\omega_{\text{TO}} = 1.495 \times 10^{14}$ rad/s, and $\Gamma = 0.9 \times 10^{14}$ rad/s.

We highlight that the Green's function appearing in Eq. (2) and detailed in Appendixes A and B explicitly contains the case $\beta = \gamma$ due to the contribution of the substrate (index s),

whereas this contribution is neglected in the vacuum contribution (index 0), so that we can write for $\beta, \gamma = 1, 2, \ldots, N$,

$$\mathbb{G}_E(\mathbf{r}_\beta, \mathbf{r}_\gamma) = \mathbb{G}_{E,s}(\mathbf{r}_\beta, \mathbf{r}_\beta)\delta_{\beta\gamma} + [\mathbb{G}_{E,0}(\mathbf{r}_\beta, \mathbf{r}_\gamma)$$
$$+ \mathbb{G}_{E,s}(\mathbf{r}_\beta, \mathbf{r}_\gamma)](1 - \delta_{\beta\gamma}). \quad (6)$$

Equation (2) can also be interpreted as one line of the block matrix equation

$$\mathbf{p} = \mathbf{p}_{\text{fl}} + \varepsilon_0 \boldsymbol{\alpha} \mathbf{E}_{\text{env}} + k_0^2 \boldsymbol{\alpha} \mathbb{G}_E \mathbf{p} \quad (7)$$

in which we define the block vectors $\mathbf{p} = (\mathbf{p}_1, \ldots, \mathbf{p}_N)^T$ and $\mathbf{E} = (\mathbf{E}(\mathbf{r}_1), \ldots, \mathbf{E}(\mathbf{r}_N))^T$ containing the dipole moments and electric fields, respectively, of each particle and the block matrices $\boldsymbol{\alpha} = \text{diag}(\alpha_1, \ldots, \alpha_N)$ and $\mathbb{G}_E$ for which each block matrix component obeys $\mathbb{G}_{E,\beta\gamma} = \mathbb{G}_E(\mathbf{r}_\beta, \mathbf{r}_\gamma)$. With that we can recast Eq. (7) in the following way:

$$\mathbf{p} = \mathbb{T}^{-1}\mathbf{p}_{\text{fl}} + \varepsilon_0 \mathbb{T}^{-1}\boldsymbol{\alpha}_{\text{CM}}\mathbf{E}_{\text{env}} \quad (8)$$

with

$$\mathbb{T}_{\beta\gamma} = [\mathbb{1} - k_0^2 \alpha_\beta \mathbb{G}_{E,s}(\mathbf{r}_\beta \mathbf{r}_\beta)]\delta_{\beta\gamma}$$
$$- k_0^2 \alpha_\beta \mathbb{G}_E(\mathbf{r}_\beta, \mathbf{r}_\gamma)(1 - \delta_{\beta\gamma}). \quad (9)$$

In the same block-matrix notation, we can now rewrite Eq. (1) for each dipole by inserting Eq. (8) as

$$\mathbf{E} = [\mathbb{1} + k_0^2 \mathbb{G}_E \mathbb{T}^{-1}\boldsymbol{\alpha}]\mathbf{E}_{\text{env}} + \mu_0 \omega^2 \mathbb{G}_E \mathbb{T}^{-1}\mathbf{p}_{\text{fl}}. \quad (10)$$

The power P_β dissipated into a given dipole $\beta = 1, 2, \ldots, N$ can be written as

$$P_\beta = \frac{1}{\pi} \int_0^\infty d\omega \, \omega \, \mathcal{C}_{pE,\beta} \quad (11)$$

$$= P_{\beta,\text{dip}\rightarrow\text{dip}} + P_{\beta,\text{back}\rightarrow\text{dip}} + P_{\beta,\text{sub}\rightarrow\text{dip}}, \quad (12)$$

and is proportional to the imaginary part of the coupled dipole-field correlation function

$$\mathcal{C}_{pE,\beta} = \sum_{i=x,y,z} \text{Im}\langle\langle p_{\beta,i} E_i^*(\mathbf{r}_\beta)\rangle\rangle. \quad (13)$$

Note that we introduced the Fourier transform $f(t) = 2\text{Re}[\int_0^\infty \frac{d\omega}{2\pi} f(\omega)e^{-i\omega t}]$. The three contributions in Eq. (12) correspond to the heat dissipated into each single dipole due to heat transfer solely between the particles themselves, heat dissipated into each dipole due to the background, and heat dissipated into each dipole in presence of the substrate, respectively. Following the method outlined in Ref. [21], each contribution can be recast under the form

$$P_{\zeta\rightarrow\text{dip},\beta} = \int_0^\infty \frac{d\omega}{2\pi} \hbar\omega \, \mathcal{T}_{\beta,\zeta\rightarrow\text{dip}} \quad (14)$$

for $\zeta \in \{\text{dip, back, sub}\}$, with the transmission coefficients

$$\mathcal{T}_{\beta,\text{dip}\rightarrow\text{dip}} = 4 \sum_{\gamma=1}^{N} \sum_{i,j=x,y,z} n_{\gamma\beta} \frac{\chi_\beta}{|\alpha_\beta|^2}[\mathbb{T}^{-1}]_{\beta\gamma,ij}$$
$$\times \chi_\gamma[\mathbb{T}^{-1\dagger}]_{\gamma\beta,ji}, \quad (15)$$

$$\mathcal{T}_{\beta,\text{back}\rightarrow\text{dip}} = 4 \sum_{\gamma,\delta=1}^{N} \sum_{i,j,l=x,y,z} n_{b\beta} \frac{\chi_\beta}{|\alpha_\beta|^2}[\mathbb{T}^{-1}]_{\beta\gamma,ij}\alpha_\gamma$$
$$\times \mathcal{C}_{b,\gamma\delta,jl} \alpha_\delta^*[\mathbb{T}^{-1\dagger}]_{\delta\beta,li}, \quad (16)$$

$$\mathcal{T}_{\beta,\mathrm{sub}\rightarrow\mathrm{dip}} = 4\sum_{\gamma,\delta=1}^{N}\sum_{i,j,l=x,y,z} n_{s\beta}\frac{\chi_\beta}{|\alpha_\beta|^2}[\mathbb{T}^{-1}]_{\beta\gamma,ij}$$
$$\times\,\alpha_\gamma\,\mathcal{C}_{s,\gamma\delta,jl}\,\alpha_\delta^*[\mathbb{T}^{-1\dagger}]_{\delta\beta,li},\tag{17}$$

and introducing the Bose-Einstein occupation probabilities

$$n_{\beta\gamma} = \frac{1}{e^{\frac{\hbar\omega}{k_B T_\beta}}-1} - \frac{1}{e^{\frac{\hbar\omega}{k_B T_\gamma}}-1},\tag{18}$$

with the reduced Planck's constant $\hbar$, the Boltzmann constant k_B, the temperature T_γ of particle γ, and the temperatures T_b and T_s of background and substrate, respectively. The remaining correlation functions $\mathcal{C}_{b/s,\beta\gamma,ij} = \langle\langle E_{i,b/s}(\mathbf{r}_\beta)E^*_{j,b/s}(\mathbf{r}_\gamma)\rangle\rangle$ are [40,41]

$$\mathcal{C}_{b,\beta\gamma,ij} = \int\frac{d^2k_\perp}{8\pi^2}e^{i\mathbf{k}_\perp(\mathbf{x}_\beta-\mathbf{x}_\gamma)}\Theta_{\mathrm{pr}}\frac{e^{-ik_z(z_\beta-z_\gamma)}}{k_z}$$
$$\times\sum_{n=s,p}(a_{n,i}^- + r_p e^{2ik_z z_\beta}a_{n,i}^+)(a_{n,j}^- + r_p^* e^{-2ik_z z_\gamma}a_{n,j}^+),$$
$$\tag{19}$$

and

$$\mathcal{C}_{s,\beta\gamma,ij} = \int\frac{d^2k_\perp}{8\pi^2}e^{i\mathbf{k}_\perp(\mathbf{x}_\beta-\mathbf{x}_\gamma)}$$
$$\times\sum_{n=s,p}\left[\Theta_{\mathrm{pr}}\frac{e^{ik_z(z_\beta-z_\gamma)}}{k_z}a_{n,i}^+ a_{n,j}^+(1-|r_n|^2)\right.$$
$$\left.+\,2\Theta_{\mathrm{ev}}\frac{e^{-|k_z|(z_\beta+z_\gamma)}}{|k_z|}a_{n,i}^+ a_{n,j}^-\mathrm{Im}(r_n)\right],\tag{20}$$

where we have introduced the projectors on the propagative and evanescent sections of the spectrum

$$\Theta_{\mathrm{pr}} = \Theta(k_0 - k_\perp),\tag{21}$$

$$\Theta_{\mathrm{ev}} = \Theta(k_\perp - k_0).\tag{22}$$

For the correlation function of the dipole moments we have used the fluctuation-dissipation theorem [21,40]

$$\langle\langle p_{\beta,i,\mathrm{fl}}p^*_{\gamma,j,\mathrm{fl}}\rangle\rangle = \hbar\varepsilon_0(1+2n_\beta)\chi_\beta\delta_{\beta\gamma}\delta_{ij}\tag{23}$$

with

$$\chi_\beta = \mathrm{Im}(\alpha_\beta) - \frac{k_0^3}{6\pi}|\alpha_\beta|^2.\tag{24}$$

Note that this is a very general formula to describe the heat flux dissipated into a collection of particles immersed in a vacuum background and in the presence of a substrate. It also allows to distinguish between the heat fluxes dissipated into each dipole meaning that we are able to discuss the spatial distribution of heat dissipated into each single dipole. In the following we will consider 1D and 2D systems and restrict ourselves to the simpler configuration of identical dipoles in the thermal-equilibrium configuration $T_1 = \cdots = T_N = T_p$, so that $P_{\mathrm{dip}\rightarrow\mathrm{dip}} = 0$ holds. At first, we will evaluate our formula in the simplest scenario of two particles: This will allow us to highlight some physical mechanisms that we will also encounter for more particles. Later, we will discuss in detail the case of a 2D disk and a 3D tip.
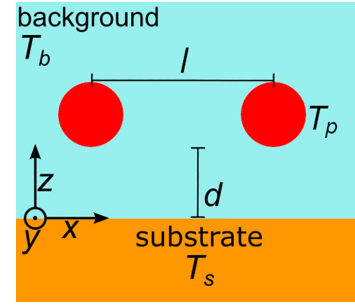

FIG. 1. Sketch of two particles with temperature $T_p = 298$ K and radius $R = 19$ nm separated by a center-to-center distance $l = 3R$ made of SiC at distance $d = 200$ nm above a SiC substrate at temperature $T_s = 323$ K immersed in a vacuum background at temperature $T_b = 293$ K.

III. TWO PARTICLES

In order to validate our model and to get some first physical insight, let us start with the configuration of two particles in free space and above a substrate, shown in Fig. 1. For the materials, we choose SiC for both the particles and the substrate, and we fix the temperatures at $T_p = 298$ K for both particles, $T_s = 323$ K for the substrate, and $T_b = 293$ K for the background. The particles are at edge-to-edge distance $d = 200$ nm from the substrate and $l = 3R$ lateral distance to each other for an identical radius of $R = 19$ nm, ensuring the validity of the dipole approximation.

From a very fundamental point of view, this situation can be compared to two harmonic oscillators of identical mass m coupled by a spring of stiffness κ, both bound to a wall with identical springs of stiffness K. This system is described by the system of differential equations

$$m\ddot{x}_{1/2} = -(K+\kappa)x_{1/2} + \kappa x_{2/1}\tag{25}$$

in which $x_{1/2}$ are the displacements of particle 1 and 2 and $\ddot{x}_{1/2}$ their second time derivatives. Rewriting this in matrix notation while making the ansatz $x_{1/2}(t) = c_{1/2}e^{i\omega t}$ yields

$$\begin{pmatrix} m\omega^2 - K - \kappa & \kappa \\ \kappa & m\omega^2 - K - \kappa \end{pmatrix}\begin{pmatrix} c_1 \\ c_2 \end{pmatrix} = \begin{pmatrix} 0 \\ 0 \end{pmatrix}.\tag{26}$$

To fulfill this equation by setting the matrix determinant to zero, one obtains two resonance frequencies, namely $\omega_1 = \sqrt{\frac{K}{m}}$ and $\omega_2 = \sqrt{\frac{2\kappa+K}{m}}$. The eigenvector $\mathbf{x}_1 = (1,1)^t$ corresponding to ω_1 describes both oscillators moving in the same direction and $\mathbf{x}_1 = (-1,1)^t$ corresponding to ω_2 describes both oscillators moving in opposite directions. While it is not straighforward to translate these quantities directly to the case of two nanoparticles described as dipoles, mainly because in the electromagnetic scenario we also have to take into account the different polarizations, we can conclude from this simple consideration that we should also find these two fundamental resonances in the spectrum of the two particles.

To show where we can find these resonances regarding our system of two dipoles, let us go back to Eqs. (1) and (2) and recast them only considering the induced dipole

moments, neglecting in other words $\mathbf{E}_{\text{env}}$ and $\mathbf{p}_{\text{fl}}$. In block matrix notation, one gets

$$\mathbf{0} = \mathbb{M}\mathbf{p}, \tag{27}$$

$$\mathbb{M} = \mathbb{1} - k_0^2 \alpha \mathbb{G}_E. \tag{28}$$

This equation demands $\det(\mathbb{M}) = 0$ in the nontrivial case. The roots of this determinant will define the resonance frequencies of the system.

A. In vacuum

We start by discussing the reference scenario of two particles in vacuum, i.e., in the absence of a substrate. In order to correctly describe the situation of an environmental field coming from both sides of the system ($z < 0$ and $z > 0$) we can take the limit in which the substrate is placed far away from the system of particles and it is replaced by an ideal blackbody. This amounts to neglect the evanescent contribution appearing in Eq. (20) and set $r_i = 0$. Under these assumptions the two correlation functions defined in Eqs. (19) and (20) are identical, as well as the heat flux from both sides towards the particles ($P_{\text{back}\to\text{dip}} = P_{\text{sub}\to\text{dip}}$). Then, Eqs. (16) and (17) give the same result for $\beta = 1, 2$ and become

$$\mathcal{T}_{\beta,\text{back/sub}\to\text{dip}} = \pi k_0^2 n_{bp} \chi_p (\mathcal{T}_{\parallel} + 2\mathcal{T}_{\perp}), \tag{29}$$

using the transmission coefficients

$$\mathcal{T}_{\parallel/\perp} = \frac{\left[1 + k_0^4 |\alpha|^2 |G_{E,\parallel/\perp}|^2\right] \frac{k_0}{6\pi} + 2k_0^2 \text{Re}[\alpha G_{E,\parallel/\perp}] \mathcal{C}_{b,12,\parallel/\perp}}{\left|1 - k_0^4 \alpha^2 G_{E,\parallel/\perp}^2\right|^2}, \tag{30}$$

with

$$G_{E,\parallel} = \frac{e^{ik_0 l}}{2\pi l} \frac{1 - ik_0 l}{k_0^2 l^2}, \tag{31}$$

$$G_{E,\perp} = \frac{e^{ik_0 l}}{4\pi l} \frac{k_0^2 l^2 + ik_0 l - 1}{k_0^2 l^2}, \tag{32}$$

and

$$\mathcal{C}_{b,11/22,ij} = \frac{k_0}{6\pi} \delta_{ij}, \tag{33}$$

$$\mathcal{C}_{b,12/21,\parallel} = \frac{\sin(k_0 l) - k_0 l \cos(k_0 l)}{2\pi k_0^2 l^3}, \tag{34}$$

$$\mathcal{C}_{b,12/21,\perp} = \frac{k_0 l \cos(k_0 l) - (1 - (k_0 l)^2 \sin(k_0 l))}{4\pi k_0^2 l^3}. \tag{35}$$

This already shows that due to the symmetry of the system the two transversal directions ($\perp$) contribute identically to the overall result while the longitudinal direction ($\parallel$) is different.

In Fig. 2 we show the spectrum of the power absorbed by both dipoles according to Eq. (29). There, we also depict the logarithm of the inverse of the determinant of the matrix defined in Eq. (28) but recast into

$$\det(\mathbb{M}) = \det(\mathbb{M}_{\perp})^2 \det(\mathbb{M}_{\parallel}), \tag{36}$$

with

$$\det(\mathbb{M}_{\perp/\parallel}) = 1 - k_0^2 \alpha G_{E,\perp/\parallel}. \tag{37}$$
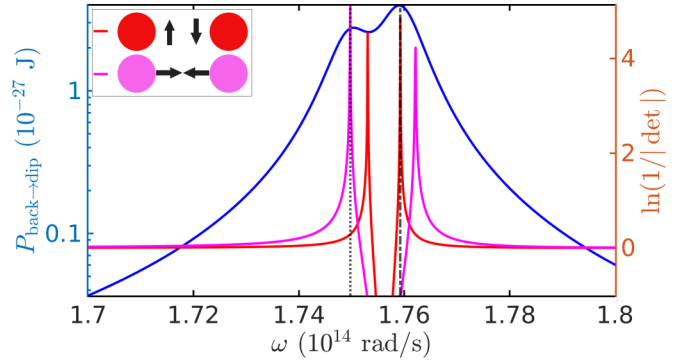

FIG. 2. Spectral heat transfer between the two particles and the background (blue) shown with the determinant of matrices $\mathbb{M}_{\perp/\parallel}$ (red/magenta) highlighting the resonance peaks for the transversal and longitudinal polarizations by the black dashed lines at $\omega_1 = 1.75 \times 10^{14}$ rad/s and $\omega_2 = 1.759 \times 10^{14}$ rad/s.

Note that the polarizability α is now a scalar because we consider identical particles. Both factors $1 - k_0^2 \alpha G_{E,\parallel/\perp}$ will exhibit two roots analogously to the model of two coupled harmonic oscillators. Obviously, the two transversal directions provide the same resonances, as mathematically described by the square. The resonances are shown in Fig. 2 by the peaks of the inverse of the determinant. One can clearly see that there are four peaks, as expected, of which only two contribute to the overall spectrum, namely the lower resonance frequency of the longitudinal modes and the higher one of the transversal modes. That is because only these "bright" modes contribute a dipole moment since they describe opposite movements as explained in the previous section [42,43]. The "dark" modes describe translations of both dipoles in the same direction, not providing a dipole moment to the overall system and thus not coupling to the electromagnetic field.

B. Above a substrate

In the presence of a substrate, the calculations become more involved because the reflected part of the Green's function in Eq. (A4) has to be considered as well. Additionally, the correlation functions also contain such a contribution taking the substrate into account. Both the reflected part of the Green's function and the two correlation functions are given for this configuration in Eqs. (B1)–(B27).

Doing the same analysis as in the previous section with respect to the determinant of matrix $\mathbb{M}$ in Eq. (28), but this time with respect to the xz components of the reflected part of the Green's function, we do not have a longitudinal mode as before for two particles in vacuum but a coupling between the longitudinal mode and the transversal one in x direction giving rise to a hybridized mode and yielding the following product of two determinants

$$\det(\mathbb{M}) = \det(\mathbb{M}_{\text{trans}})\det(\mathbb{M}_{\text{mix}}), \tag{38}$$

with

$$\det(\mathbb{M}_{\text{trans}}) = \left(1 - k_0^2 \alpha G_{E,s,\perp}^{\text{id}}\right)^2 - k_0^2 \alpha \left(G_{E,s,y}^{\text{dif}} + G_{E,\perp}\right)^2, \tag{39}$$
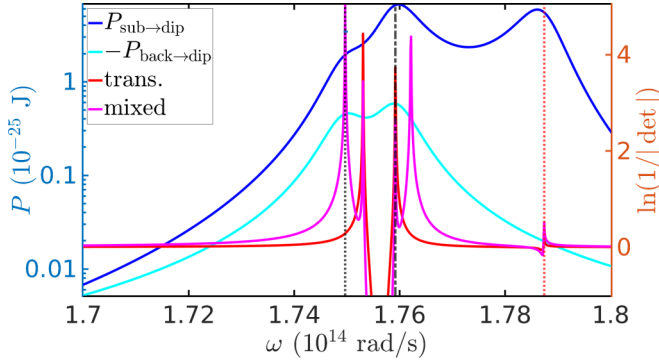
FIG. 3. Spectral heat transfer between the two particles and the substrate (dark blue) or the background (light blue) shown with the determinant of matrices $\mathbb{M}_{\perp/\mathrm{mix}}$ (red/magenta) highlighting the resonance peaks for the transversal and mixed polarizations by the black and red dashed lines at $\omega_1 = 1.75 \times 10^{14}$ rad/s, $\omega_2 = 1.759 \times 10^{14}$ rad/s, and $\omega_{\mathrm{SPhP}} = 1.787 \times 10^{14}$ rad/s.

and

$$
\begin{aligned}
\det(\mathbb{M}_{\mathrm{mix}}) = &\left[\alpha^2 k_0^4 G_{E,s,\mathrm{mix}}^2 - \left(1 - \alpha k_0^2 \left(G_{E,s,x}^{\mathrm{dif}} + G_{E,\parallel}\right)\right)\right. \\
&\times \left.\left(1 + \alpha k_0^2 \left(G_{E,s,z}^{\mathrm{dif}} - G_{E,\perp}\right)\right)\right] \\
&\times \left[\alpha^2 k_0^4 G_{E,s,\mathrm{mix}}^2 - \left(1 - \alpha k_0^2 \left(G_{E,s,z}^{\mathrm{dif}} + G_{E,\perp}\right)\right)\right. \\
&\times \left.\left(1 + \alpha k_0^2 \left(G_{E,s,x}^{\mathrm{dif}} - G_{E,\parallel}\right)\right)\right].
\end{aligned}
\tag{40}
$$

Due to the coupling, the determinant of $\mathbb{M}_{\mathrm{mix}}$ has now four roots.

The results for the heat exchange between the two particles and the background as well as with the substrate are shown in Fig. 3. Note that, due to our choice of temperatures, the spectral power between particles and background is negative. Therefore, we show $-P_{\mathrm{back}\to\mathrm{dip}}$ instead. The spectrum for the heat flux between the particles and the background (light blue) looks the same as in Fig. 2 apart from an overall amplification. The spectral peaks for this contribution are at the same positions as for the case without substrate and can also be found in the heat flux between the particles and the substrate (dark blue). As shown by the inverse determinants, these resonance frequencies correspond to two roots of the determinant. The fact of not seeing all of them through a contribution to the spectral flux can be attributed to the existence of dark and bright modes as in the case without substrate.

In addition to these two peaks for both spectral heat fluxes, there is also a third peak in the spectral heat flux between the dipoles and the substrate. It corresponds to the well known resonance frequency of the surface phonon polariton (SPhP) of SiC at $\omega_{\mathrm{SPhP}} = 1.787 \times 10^{14}$ rad/s at which the parallel polarized reflection coefficient in Eq. (A8) has a maximum due to $\varepsilon_{\mathrm{sub}}(\omega_{\mathrm{SPhP}}) \approx -1$. Since this mode characterizes a strong coupling between substrate and particles, it can only be found in the heat flux between the dipoles and the substrate and not in the one with the background. Note that both determinants also exhibit a root at ω_{SPhP} due to the inclusion of the reflected part of the Green's function.

Translating these validations for two particles to the upcoming case of a 2D disk, there will be resonances stemming from the eigenmodes of the disk itself which coincide with
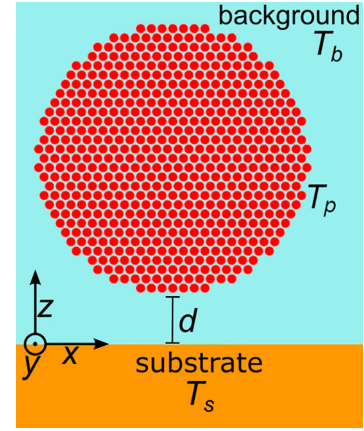

FIG. 4. Sketch of a 2D disk with radius $R = 500$ nm at temperature $T_p = 298$ K at distance $d = 200$ nm above a SiC substrate at temperature $T_s = 323$ K immersed in a vacuum background at temperature $T_b = 293$ K. All $N = 583$ particles have a radius of $r = 19$ nm and are made of SiC.

the case without substrate. In the spectral heat flux between the particles and the substrate there will be a peak at ω_{SPhP} which will dominate for the near field due to its evanescent character.

IV. 2D DISK

After studying the very idealized system made of two point particles, we now move to a more realistic scenario of an extended system. To this aim, we consider in this section a 2D disk of radius $R = 500$ nm as depicted in Fig. 4. In this first application we limit ourselves to a 2D geometry for several reasons. First, this allows to fill it with small dipolar particles while keeping the computational time reasonable. Also, the study of what happens within the transition from a partially filled disk (a ring) to a full disk is more feasible. Finally, the connection between spatial power distribution obtained within our model and field modes existing in the system can be studied more easily, since the representation of field modes is much easier in a 2D system. A 3D geometry mimicking the tip-substrate geometry employed in several experiments will be presented in Sec. V.

In the following simulations, the parameters for background and substrate remain the same as before. The particles are identical in temperature $T_p = 298$ K, radius $r = 19$ nm, and both particles and substrate are made of SiC. In order to fill a disk of given radius R as densely as possible with nanoparticles we consider a close-packing arrangement and keep only the nanoparticles which are fully inside the surface of the disk. Using this approach, a disk completely filled with particles corresponds to $N = 583$ particles. The radius r in with respect to radius R is chosen such that $Nr^2/R^2 = 0.84$. For comparison, this ratio is $Nr^2/R^2 = 0.9$ for $r = 3$ nm and $N = 24\,895$ so that the chosen radius of $r = 19$ nm already represents a disk whose surface area is almost completely filled by dipoles and, therefore, provides a reasonable approximation of the disk geometry in the spirit of DDA.
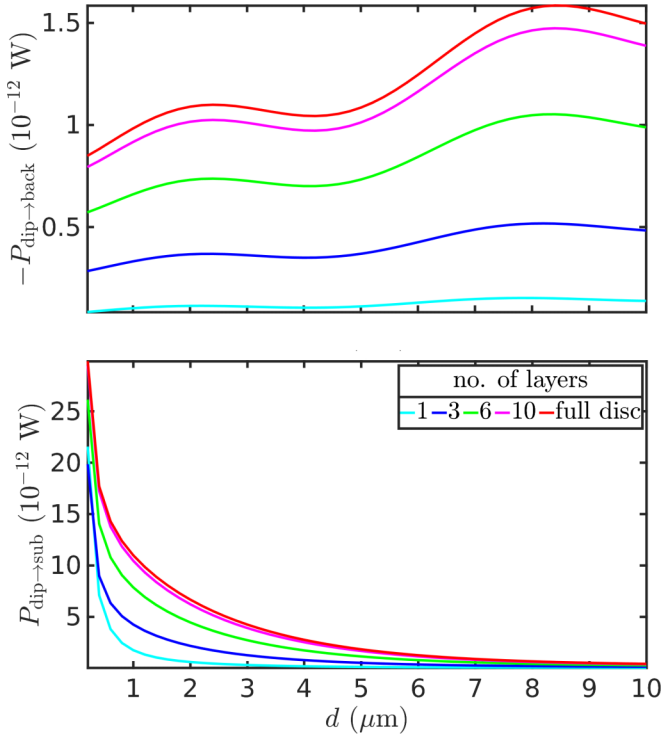
FIG. 5. $-P_{\text{back} \to \text{dip}}$ (a) and $P_{\text{sub} \to \text{dip}}$ (b) for different numbers of layers starting with one ring on the outside and adding more towards the inside until we obtain a full disk.

In Fig. 5 we show on the total power

$$P_{\zeta \to \text{dip}} = \sum_{\beta=1}^{N} P_{\beta, \zeta \to \text{dip}}, \quad (41)$$

for $\zeta \in \{\text{back}, \text{sub}\}$ absorbed by the system of N dipoles and show both contributions $-P_{\text{back} \to \text{dip}}$ and $P_{\text{sub} \to \text{dip}}$ while varying the distance between the disk and the substrate for different amounts of layers starting with only a ring of particles on the outside of the disk in Fig. 4 and adding more rings towards the inside until we end up with the full disk. One can clearly see that $P_{\text{sub} \to \text{dip}}$ dominates in the near field and up to distances $d < 6$ μm. This distance also coincides with the coherence length of the SPhP mode of the SiC substrate which is the dominating coupling mechanism in the near field between substrate and particles. On the contrary, in the far-field regime $P_{\text{back} \to \text{dip}}$ becomes more important, resulting in a sign flip for the total received flux. Let us also stress that because of the nonmonotonic behavior of $P_{\text{back} \to \text{dip}}$, due to interference between the radiation directly emitted away from substrate and particles and the one reflected at the substrate, this nonmonotony will be imprinted on the overall result in the far field as a signature of this contribution because $P_{\text{sub} \to \text{dip}}$ is decaying exponentially. $P_{\text{back} \to \text{dip}}$ also increases for larger distances showing an attenuation effect due to coupling to the substrate. Note that this increase for $P_{\text{back} \to \text{dip}}$ in absolute values will asymptotically reach the blackbody limit for even larger distances. Additionally, we want to stress that although all curves share indeed a the same qualitative behavior, the ratio between them does not coincide with the ratio of the number of particles involved in each configuration.

From a numerical point of view it is also interesting to note that $P_{\text{sub} \to \text{dip}}$ converges faster towards the result of the full disk, which happens already for nine layers, than $P_{\text{back} \to \text{dip}}$ for which 11 layers are required, which corresponds to all particles but the seven at the center of the disk. Especially in the near field in which $P_{\text{sub} \to \text{dip}}$ dominates, one could reduce the computation time by taking less layers into account. Nevertheless, we will see later that this does not hold for a qualitative discussion because the different configurations will have strikingly different spatial power distributions.

A. Spatial power distribution

Now, we want to turn to the spatial distribution of the heat fluxes. Again, we will look at the evolution of a ring of particles towards the full disk to see whether certain particles or regions are more important than others. The parameters are as before. We consider three different distances between the (layered) disk and the substrate to cover the near field ($d = 200$ nm), the far field ($d = 10$ μm), and the intermediate regime ($d = 1$ μm). Here we restrict ourselves to three figures for the setup of only one outer ring, a crown of four layers, and the full disk [44].

Let us start with the description of panels (d)–(f) of Figs. 6–8, corresponding to the heat flux between particles and substrate. In all configurations one can clearly see for $d = 200$ nm that the particles close to substrate (bottom) experience the largest flux from the substrate. This is clearly a signature of the SPhP mode due to the strong coupling in this near-field regime. For larger distances d this signature vanishes and we are left with bright spots in the middle. This is reminiscent of configurational modes of each disk layout in accordance to our findings for two particles in Sec. III, and suggests that here we are indeed observing an indirect evidence of eigenmodes of the ring, crown, and disk, respectively. Interestingly, we can also find bright spots at the bottom if we stay below four layers in the intermediate regime. The bright spot at the bottom, then, smears out towards the middle and center. This is clearly a many-body effect due to more particles that can couple with each other and distribute the incoming heat flux from the substrate for more particle layers. For less layers the closest particles still obtain more heat due to evanescent waves like frustrated modes in this intermediate regime. Due to poorer coupling, especially in the case of a single layer where there are only two nearest neighbors for each particle, the bottom part still obtains much more power than the upper part. Nevertheless, the eigenmode signature dominating in the far field can be already seen for configurations with less than four layers. This already represents a competition between the SPhP mode and the configurational eigenmodes of the system.

Panels (a)–(c) of Figs. 6–8, corresponding to the heat flux between particles and background, are also worth discussing because it shows counter-intuitive behavior. First, the upper part of the ring, crown, and disk emits more heat in the near-field regime for each configuration. For less layers this is more strictly bound to the very top and smears out again for more layers until we find brighter spots in the middle and center but still the upper part emits more power than the lower part. This shows that the substrate attenuates heat transfer towards
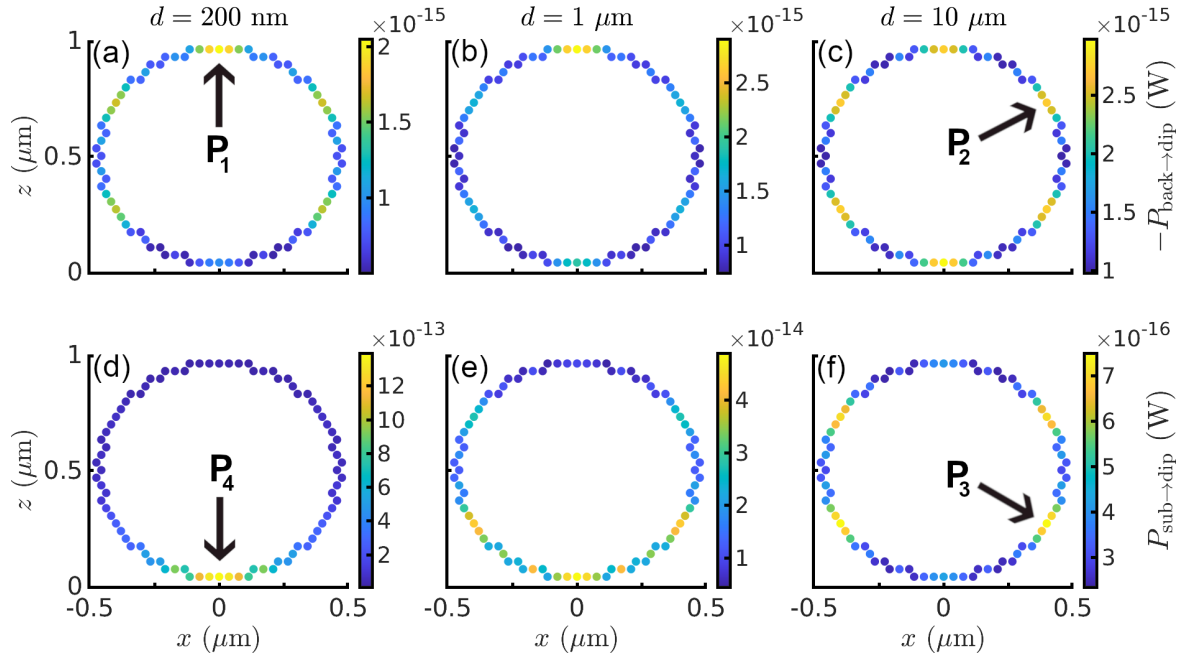
FIG. 6. Spatial power distribution for one layer. [(a)–(c)] Heat flux between particles and background. [(d)–(f)] Heat flux between particles and substrate. The columns correspond to three different distances given above the upper panel. For better reference in Sec. IV B 2 we already highlight the particles of concern for later spectral analysis by P_1-P_4.

the background due to coupling which is stronger for particles closer to the substrate. Interestingly, this brighter upper part is even more pronounced for the intermediate regime in all configurations. In the far field we expect again the eigenmodes to dominate the spectrum to whom we ascribe the spatial distribution of $P_{\text{back}\rightarrow\text{dip}}$ for each configuration. In the intermediate regime we would have expected something between near and far field meaning that the upper part is still more pronounced but also a stronger signature of the eigenmodes. This could,

for example, hint towards the influence of frustrated modes. As another interesting feature, we find in the far field that the lower part for configurations with less than four layers is more pronounced than the upper region.

We stress the presence of the bright spots at the center which always occur apart from the cases of only a few layers and from $P_{\text{sub}\rightarrow\text{dip}}$ in the near field. This is, as we will show later in more detail, related to the eigenmodes of the configuration which is even an important feature if we only
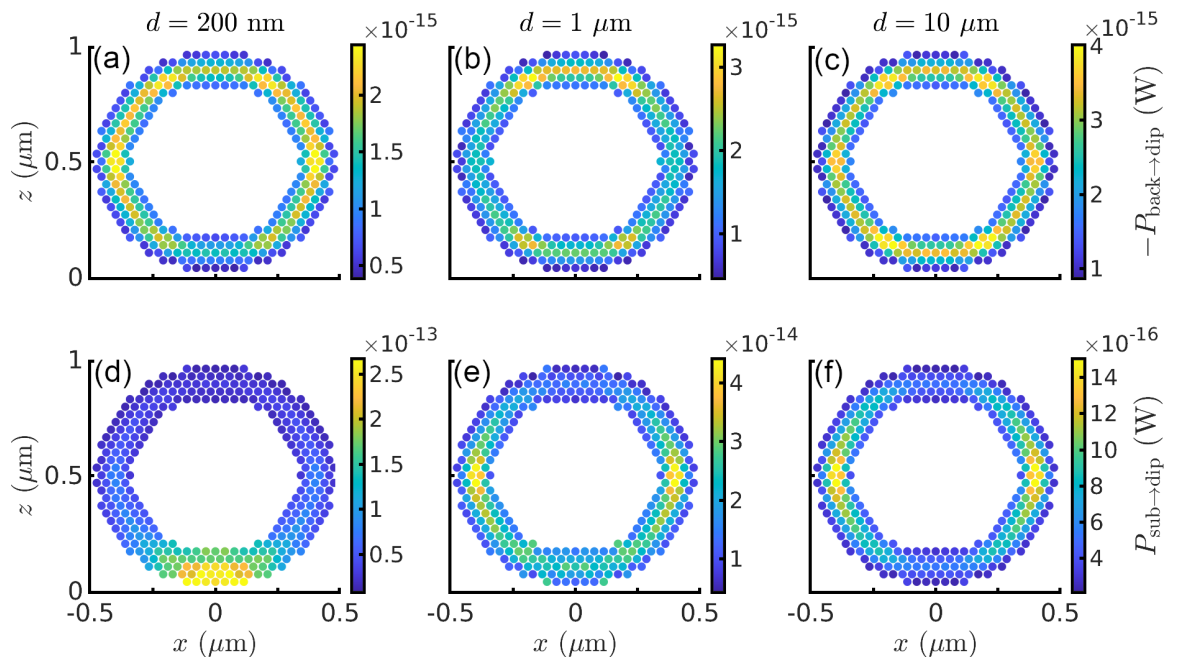

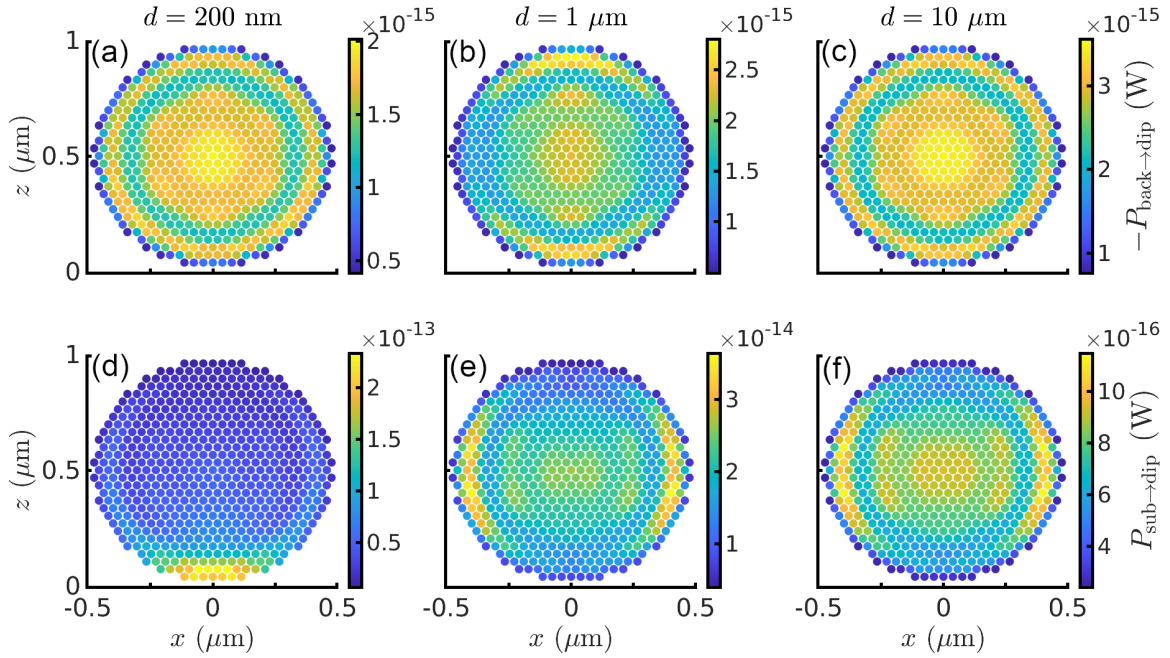FIG. 7. Spatial power distribution for four layers.

FIG. 8. Spatial power distribution for the full disk.

remove the central particle of the full disk. Additionally, it is important to stress the exception for configurations with only a small number of layers. For less than four layers there are many striking differences. To show the mechanisms behind this spatial power distribution, we will now analyze these configurations spectrally.

B. Spectral analysis of the dissipated power

As we did before for the two-particle case, we will now discuss the spectra for different configurations: a ring ($N = 84$ particles, one layer), a crown ($N = 318$, four layers), and the full disk ($N = 583$). The spectra are shown in Fig. 9. In the left column, panels (a), (c), and (e) show the spectral heat flux between particles and background $P_{\text{back} \to \text{dip}}$ and panels (b), (d), and (f) in the right column the one between the particles and the substrate $P_{\text{sub} \to \text{dip}}$. Everything is shown for the three regimes: near field, far field, and intermediate regime. For $P_{\text{back} \to \text{dip}}$ we find either two [Figs. 9(a) and 9(e)] or three [Fig. 9(c)] major resonance peaks which are highlighted in Fig. 9 by the arrows. We can also find the same resonances in $P_{\text{sub} \to \text{dip}}$ together with an additional peak at ω_{SPhP} (red dashed line) which surpasses the other ones in the near field. Since we can see in each panel in Fig. 9 that this peak dominates in the near field and vanishes in the far field, this proves the strong influence of the coupling between the dipoles of each configuration and the SPhP mode of the substrate. As expected, the eigenmodes of the configuration dominates in the far field for $P_{\text{sub} \to \text{dip}}$ and the overall spectral amplitude goes down as shown in Fig. 5. In the case of $P_{\text{back} \to \text{dip}}$, the spectrum behaves vice versa regarding that distance dependence as explained in the previous section due to a decreasing attenuation due to coupling with the substrate. Interestingly, the peak at the largest frequency is always more pronounced for the intermediate regime compared to the other two regimes. We also relate this to our observation that the intermediate regime has

a different spatial distribution for $P_{\text{back} \to \text{dip}}$. For completeness, we also show by the black dashed line the resonance frequency of a single spherical SiC particle at which $\varepsilon_{\text{SiC}} = -2$ holds. It is clear that this frequency does not play a significant role in the overall spectrum.

1. Spectrum of a ring with and without substrate

In Fig. 10 we show the same as in Figs. 9(a) and 9(b) for $d = 200$ nm in comparison with the case without substrate. Let us first of all stress that we can identify all resonances with roots of the determinant in Eq. (28). However, since we
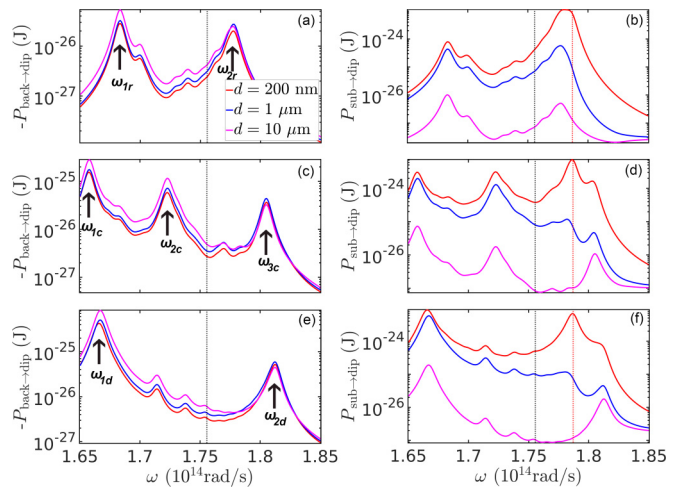

FIG. 9. Spectral heat flux between the particles and the background (left, turned positive) and the substrate (right) for three different distances to the substrate. [(a) and (b)] One layer. [(c) and (d)] Four layers. [(e) and (f)] Full disk. Additionally, we show the frequencies corresponding to $\varepsilon_{\text{SiC}} = -1$ (red dashed) and $\varepsilon_{\text{SiC}} = -2$ (black dashed). All parameters as before.
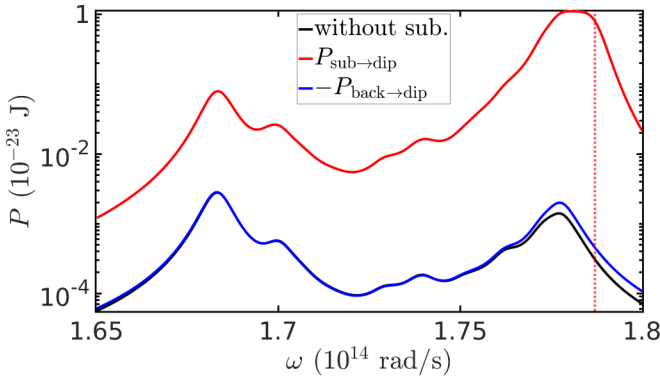
FIG. 10. Comparison of the spectral heat fluxes between particles and background (blue) and substrate (red) with the case without substrate (black). The distance between the ring and the substrate is fixed to $d = 200$ nm. All other parameters as before.

have 84 particles for this configuration, we could in principle have 232 different roots in the determinant so that it is not easy to connect each root to one resonance but rather clusters of roots. Comparing all three graphs, one can also clearly see that, apart from the peak highlighted by the red dashed line, all resonances stem from the eigenmodes of the ring since they also appear in the case without substrate. At the red dashed line the SPhP mode has a strong influence on the spectral heat flux between dipoles and substrates.

Interestingly, $P_{\text{back}\rightarrow\text{dip}}$ differs significantly from the case without substrate at the peak at $\omega = 1.777 \times 10^{14}$ rad/s. We conclude, therefore, that the substrate can enhance this resonance which we also showed in Fig. 9(a) while noticing that this enhancement is particularly important in the intermediate regime of $d = 1$ μm. To go further into details we will now focus on different particles on the ring for further spectral analysis.

2. Special particles on a ring

For the ring configuration we compare the spectra of four particles that are highlighted in red in the legend of Fig. 11. We compare three different distances, one for each regime, for $P_{\text{back/sub}\rightarrow\text{dip}}$ [Figs. 11(a), 11(c) and 11(e)/11(b), 11(d), and 11(f)]. As a reference, we also put the spectrum for the sum over all particles of the disk in red. The four particles correspond to the one at the top (P_1), two ones that are close to the middle (P_2 and P_3), and one at the very bottom close to the substrate (P_4), as already depicted in Fig. 6.

For $P_{\text{sub}\rightarrow\text{dip}}$, the red dashed line highlights ω_{SPhP}. At this frequency we clearly observe a strong resonance for the particle close to the substrate (P_4) followed by the one in the
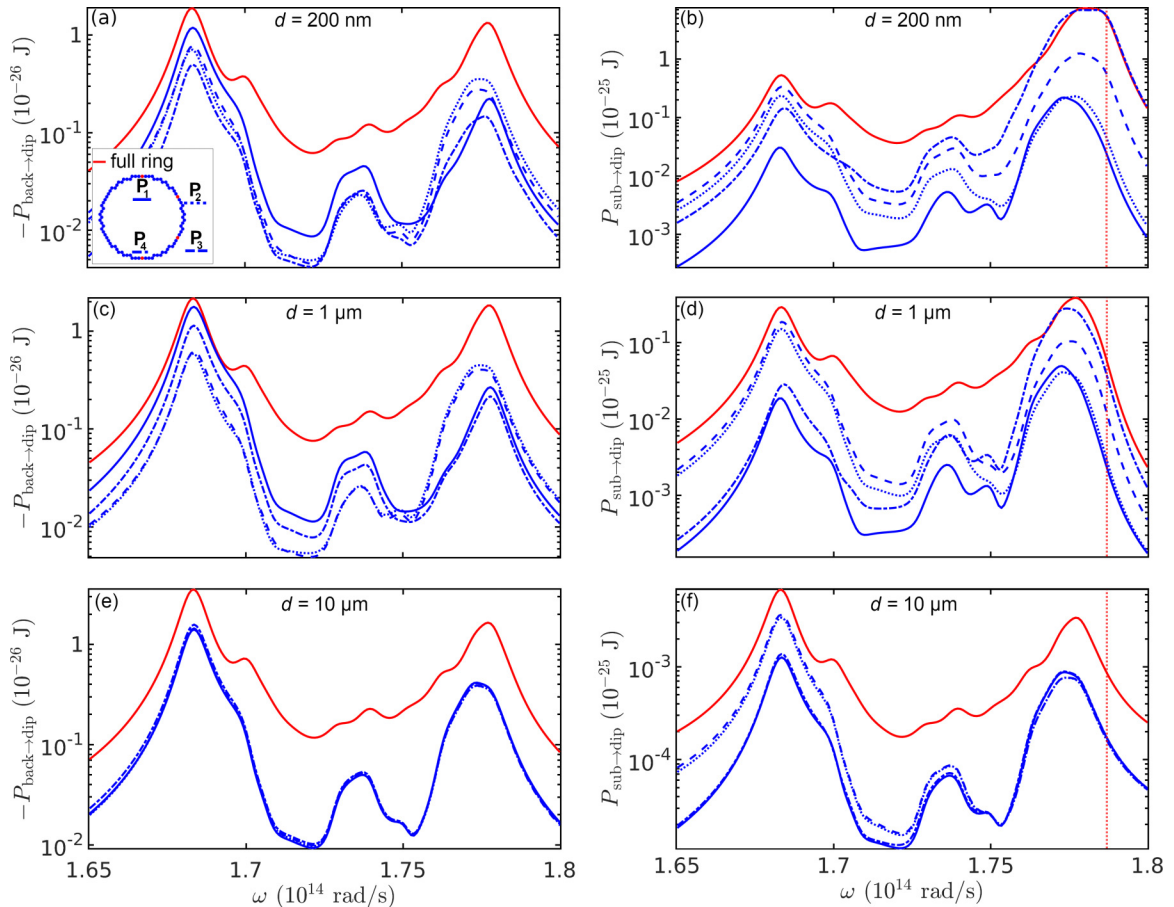

FIG. 11. Comparison of the spectral heat fluxes between certain particles (see legend and Fig. 6) and background [(a), (c), and (e)] and substrate [(b), (d), and (f)] for different particles (blue) and the sum of all particles on the ring divided by 15 (red). ω_{SPhP} is highlighted by the red dashed line at the bottom. All parameters as before.
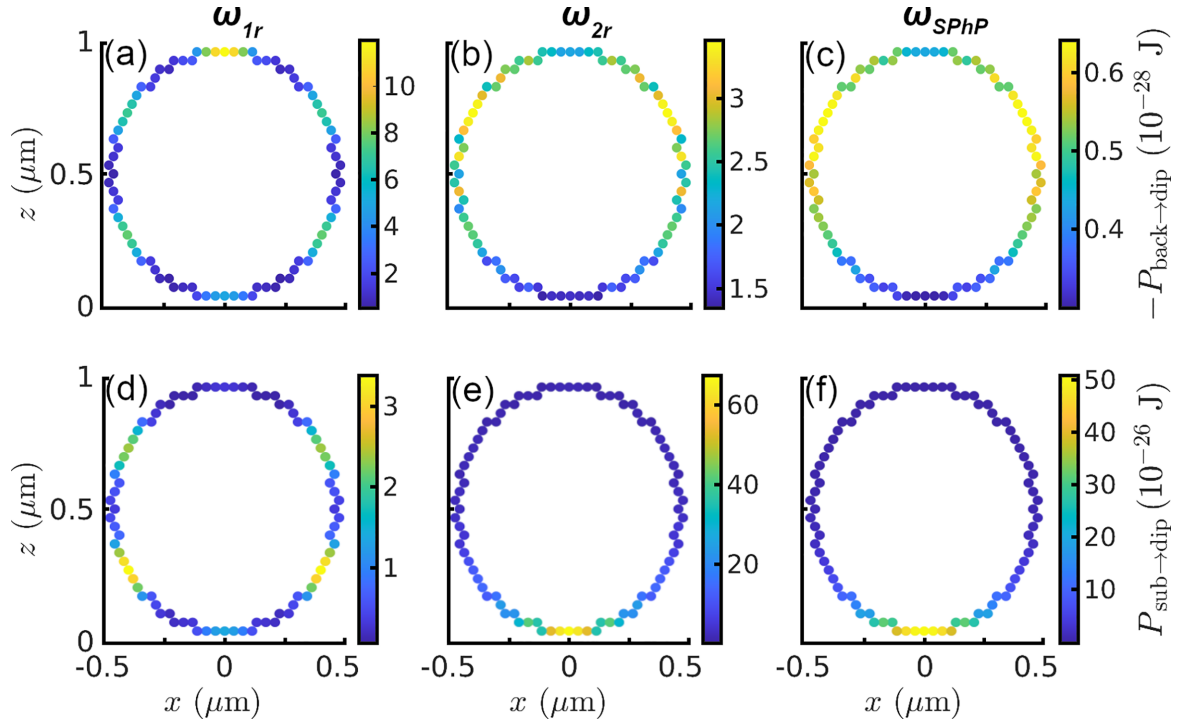
FIG. 12. Spatial distribution of the spectral heat fluxes between particles and background [(a)–(c)] and substrate [(d)–(f)] for different frequencies indicated above the upper panel for the ring configuration (one layer). The distance between the ring and the substrate is fixed to $d = 200$ nm. The frequencies are the ones highlighted in Fig. 9. All other parameters as before.

middle that is closer to the substrate (P_3) in the near-field in Fig. 11(b). The difference in amplitude is getting less for larger distances and seems to vanish in the far field, which is not surprising in the context of the SPhP mode coupling between substrate and particles. The resonance at $\omega_{1r} = 1.683 \times 10^{14}$ rad/s seems to favor the particles closer to the center. For larger distances this favoring is even more obvious. This explains why we see these particles as bright spots in Fig. 6 in the far field.

For $P_{\text{back}\rightarrow\text{dip}}$ we do not observe many differences in the far field; all graphs almost overlap. In the intermediate regime and in the near field, however, the top particles exhibits the strongest resonance at ω_{1r} and remains dominating up until close to ω_{2r} which is where the middle particles become more important. Note that at this frequency for the intermediate regime $d = 1$ μm, the difference between the centered particles (P_2 and P_3) and the top particle (P_1) increases which coincides with the inversion of graphs for different distances in Figs. 9(a), 9(c) and 9(e) at this frequency. Finally, we will show the influence of the configurational modes and the SPhP mode spatially.

3. Spatial distribution for special frequencies

Let us finally look at the spatial distribution of the heat fluxes $P_{\text{back/sub}\rightarrow\text{dip}}$ for different frequencies corresponding to the major peaks highlighted in Fig. 9 for the cases of the ring ($N = 84$ particles, one layer, Fig. 12), a crown ($N = 318$, four layers, Fig. 13), and the full disk ($N = 583$, Fig. 14). The calculations for all figures are performed for $d = 200$ nm.

For the ring we see the largest heat flux $P_{\text{back}\rightarrow\text{dip}}$ at ω_{1r} at the top particle which is due to the eigenmodes of the

ring being less attenuated there. For the other two frequencies we observe the eigenmode signature attenuated for particles closer to the substrate and also the top particles as described in the previous section. For ω_{SPhP} and ω_{2r} the heat flux $P_{\text{sub}\rightarrow\text{dip}}$ is the most pronounced at the bottom particle due to strong coupling due to the SPhP mode and evanescent modes in general. At ω_{1r} we re-encounter the eigenmode signature enhanced for particles closer to the substrate.

For the cases of a crown in Fig. 13 and a disk in Fig. 14 we observe a similar behavior. The SPhP mode has a clear signature by enhancing the $P_{\text{sub}\rightarrow\text{dip}}$ for the bottom particles. For the other frequencies we always find the signature of an eigenmode that is enhanced for the bottom particles due to evanescent waves. For $P_{\text{back}\rightarrow\text{dip}}$ we also clearly see the eigenmodes of the system but attenuated at the bottom part due to coupling with the substrate. Especially for the full disk the different spatial distribution for each eigenmode is well visible. The only exception is the case of ω_{1d} for the full disk where we see brighter spots closer to the substrate.

Conclusively, this shows the "competition" between the eigenmodes of the configuration and the coupling with substrate which either enhances the heat flux especially at the SPhP mode or attenuates it for the heat flux between particles and background.

V. TIP GEOMETRY

The two previous sections showed the influence of the main physical mechanism involved in the heat transfers between substrate, dipoles, and background in increasingly more complex geometries. In this section, we want to apply our theoretical framework to a more practical geometry which
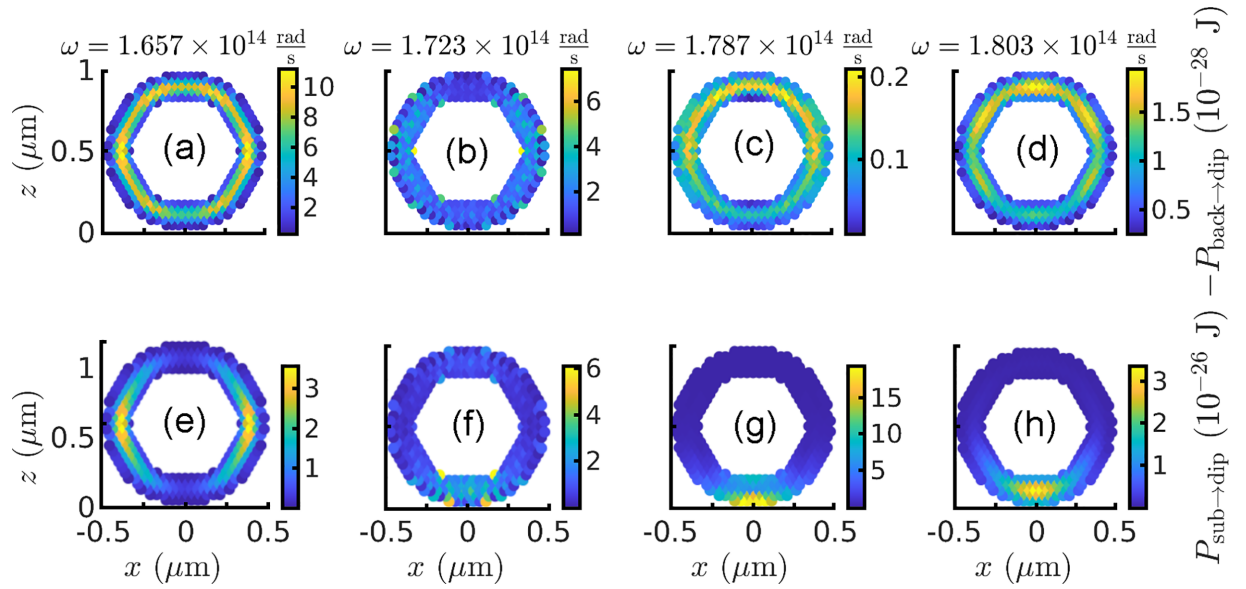
FIG. 13. As in Fig. 12 but for a crown configuration (four layers).

is often used in thermal near-field microscopy. For a wide variety of near-field experiments, a sharp tip, e.g., provided by the cantilever of an atomic force microscope, is brought in the vicinity of a sample surface to scan it and either measure the heat transfer between sample and tip [4,5] or the thermal radiation scattered by the tip [6–8]. From a theoretical point of view, it is interesting to know how accurate the modeling of the geometrical shape of the tip has to be to take into account all particles that are most involved in the heat transfer. Is it, for instance, sufficient to approximate the tip by a single

dipole corresponding to the tip apex because only the front part is important due to surface modes which dominate the near field? We will now use a tiplike geometry approximated by SiC dipoles at distance $d = 100$ nm above a SiC substrate. The tip is modeled by a cone of hight $H = 1$ μm and an opening angle of $\alpha = 30°$ which is filled by $N = 526$ particles of a radius of $r = 45$ nm. This is shown in Fig. 15. For the temperature assignment we chose the same ordering as for the disk such that the particles constituting the tip have a uniform temperature distribution of $T_p = 298$ K. The background is
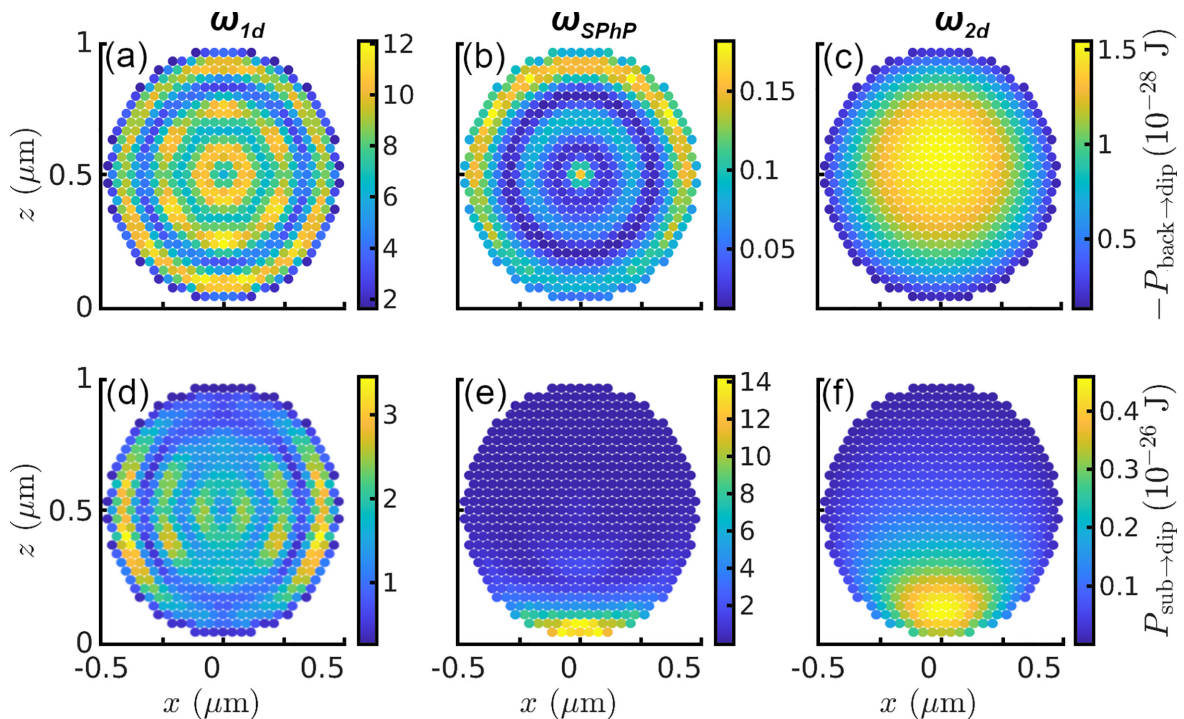

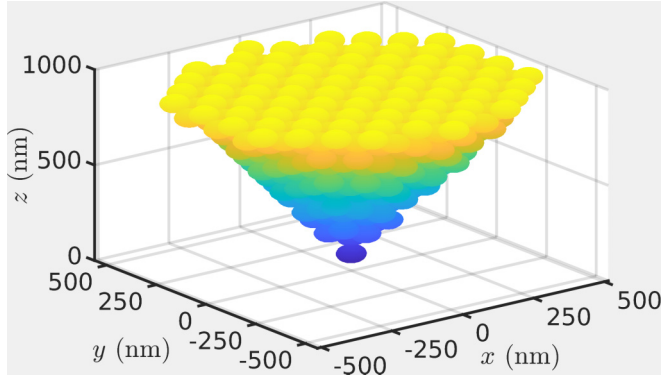FIG. 14. As in Fig. 12 but for the full disk.

FIG. 15. Tip modeled by a cone of hight $H = 1$ µm and opening angle $\alpha = 30°$ filled by $N = 526$ particles of radius $R = 45$ nm.

held at $T_b = 293$ K and the substrate at $T_s = 323$ K. Dipoles and substrate are made of SiC.

In Fig. 16 we show the tomography of the tip in Fig. 15 corresponding to the y-z plane at $x = 0$. Both contributions $P_{\text{back/sub}\rightarrow\text{dip}}$ show that the front part is the most important for the heat transfer. On the other hand, Fig. 16(b) reveals that it is not the front most particle obtaining the most heat from the substrate due to the surface mode at ω_{SPhP} but the second closest one. This is in contrast to the case of only two particles vertically aligned over a substrate surface for which the closest particle obtains the most thermal radiation which we show in the inset for identical particles and temperatures compared to the tip model. This highlights the importance of the other surrounding particles constituting the tip whose complex N-body interactions with the front particles have a high impact on the power distribution. The physical mechanisms behind this feature have been explained in the previous sections which have now to be translated to 3D, namely the surface mode and the eigenmodes of the tip geometry.

In Fig. 16(a) we also show the heat flux between the background and the dipoles. There, the front part is most important for the heat transfer as well but noticeably the outer particles also emit more heat than the particles at the center. This, again, reflects a mix of the attenuation by the substrate and the influence of the eigenmodes. Due to the attenuation, also the
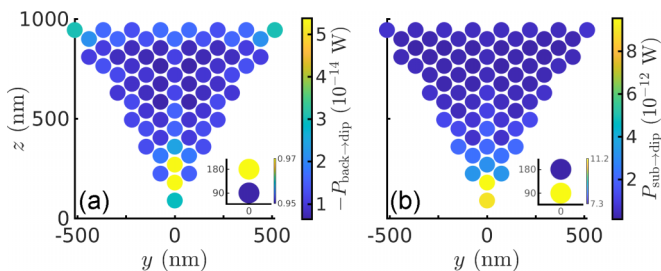

FIG. 16. Tomography over the y-z plane of the tip in Fig. 15 made of SiC at $d = 100$ nm above a SiC substrate for the same temperature assignment as for the disk with a uniform temperature distribution for the particles constituting the tip. We show the heat transfer between background and dipoles (a) and between substrate and dipoles (b) compared to two vertically aligned particles of the same size and temperature in the insets.

more removed particle for a corresponding vertically aligned two-particle chain emits more heat towards the background. Hence, in contrast to $P_{\text{sub}\rightarrow\text{dip}}$, for the tip $P_{\text{back}\rightarrow\text{dip}}$ reflects the usual findings of a particle chain. However, both contributions show that an approximation of the front-most part of the tip by a single dipole would lack the influence of the surrounding particles which have an even higher impact on the heat transfer.

Note that the dissipated power density, to some extend, can be related to the local density of states (LDOS). Experiments with a probing tip, which we geometrically approximated by dipoles in this section, that directly measure the spatial distribution of the LDOS could benefit from this method, like it was recently done but for another range of frequencies [45,46]. In plasmonic systems the LDOS can be measured by electron-energy-loss spectroscopy [47] which cannot be translated to polar systems. However, the local change of the LDOS could be characterized by measuring spontaneous emission of quantum dots [48] and the decay rates of molecules [49] placed next to the probing tip or on the probing tip itself.

VI. CONCLUSION

By performing a tomographic analysis of radiative heat transfers between an object, a substrate, and its thermal environment, we have demonstrated the crucial role played by many-body interactions in near-field regime and highlighted the intimate connection which exists between power distribution and eigenmodes within a solid. Our study sheds light on the fundamental mechanisms driving heat exchanges between mesoscopic objects and their surrounding environment. Our study paves the way to a rational design of local hot spots at a deep subwavelength scale by exploiting shape optimization of solids which will require a coupling between the DDA method and conduction within each solid. This could lead to important implications in the fields of nanoscale thermal management, heat-assisted data recording, and nanoscale thermal imaging.

ACKNOWLEDGMENTS

APPENDIX A: GENERAL GREEN'S FUNCTIONS AND CORRELATION FUNCTIONS

As mentioned in Sec. II, the Green's function for each particle consists of a vacuum part and a reflected part due to the presence of the substrate [50]. In Eq. (6) this is described more explicitly. Throughout this work, we use the vacuum Green's function

$$\mathbb{G}_{E,0}(\mathbf{r}, \mathbf{r}')$$

$$= \frac{e^{ik_0\rho}}{4\pi\rho}\left[\frac{k_0^2\rho^2 + ik_0\rho - 1}{k_0^2\rho^2}\mathbb{1} - \frac{k_0^2\rho^2 + 3ik_0\rho - 3}{k_0^2\rho^2}\hat{\boldsymbol{\rho}} \otimes \hat{\boldsymbol{\rho}}\right]$$

$$\tag{A1}$$

with

$$\hat{\boldsymbol{\rho}} = \frac{\mathbf{r} - \mathbf{r}'}{|\mathbf{r} - \mathbf{r}'|}, \tag{A2}$$

$$\rho = |\mathbf{r} - \mathbf{r}'|. \tag{A3}$$

For the reflected contribution, we employ the following expression:

$$\mathbb{G}_{E,s}(\mathbf{r}, \mathbf{r}') = \int \frac{d^2 k_\perp}{(2\pi)^2} e^{i\mathbf{k}_\perp \cdot (\mathbf{x} - \mathbf{x}')} \frac{i e^{ik_z(z+z')}}{2k_z} \sum_{n=s,p} r_i \mathbf{a}_i^+ \otimes \mathbf{a}_i^- \tag{A4}$$

with the polarization unit vectors

$$\mathbf{a}_s^\pm = \frac{1}{k_\perp}(-k_y, k_x, 0)^t, \tag{A5}$$

$$\mathbf{a}_p^\pm = \frac{1}{k_\perp k_0}(\pm k_x k_z, \pm k_y k_z, -k_\perp^2)^t, \tag{A6}$$

and the Fresnel amplitude reflection coefficients

$$r_s = \frac{k_z - k_{z,\text{sub}}}{k_z + k_{z,\text{sub}}}, \tag{A7}$$

$$r_p = \frac{\varepsilon_{\text{sub}} k_z - k_{z,\text{sub}}}{\varepsilon_{\text{sub}} k_z + k_{z,\text{sub}}}. \tag{A8}$$

Therein, we used the definitions

$$\mathbf{k}_\perp = (k_x, k_y)^t, \tag{A9}$$

$$\mathbf{x} = (x, y)^t, \tag{A10}$$

$$d^2 k_\perp = dk_x dk_y, \tag{A11}$$

$$k_z = \sqrt{k_0^2 - k_\perp^2}, \tag{A12}$$

$$k_{z,\text{sub}} = \sqrt{\varepsilon_{\text{sub}} k_0^2 - k_\perp^2}. \tag{A13}$$

APPENDIX B: GREEN'S FUNCTION AND CORRELATION FUNCTIONS FOR TWO PARTICLES ABOVE A SUBSTRATE

The reflected part of the Green's function in Eq. (A4) simplifies for two particles as in Fig. 1 to

$$\mathbb{G}_{E,s}(\mathbf{r}_{1/2}, \mathbf{r}_{1/2}) = G_{E,s,\perp}^{\text{id}}(\hat{\mathbf{x}} \otimes \hat{\mathbf{x}} + \hat{\mathbf{y}} \otimes \hat{\mathbf{y}}) + G_{E,s,z}^{\text{id}} \hat{\mathbf{z}} \otimes \hat{\mathbf{z}} \tag{B1}$$

with

$$G_{E,s,\perp}^{\text{id}} = i \int_0^\infty \frac{dk_\perp k_\perp}{8\pi k_z} e^{2ik_z(d+R)} \left[r_s - r_p \frac{k_z^2}{k_0^2} \right], \tag{B2}$$

$$G_{E,s,z}^{\text{id}} = i \int_0^\infty \frac{dk_\perp k_\perp^3}{4\pi k_0^2 k_z} e^{2ik_z(d+R)} r_p, \tag{B3}$$

if both spacial arguments of the Green's function are identical and to

$$\mathbb{G}_{E,s}(\mathbf{r}_{1/2}, \mathbf{r}_{2/1}) = G_{E,s,x}^{\text{dif}} \hat{\mathbf{x}} \otimes \hat{\mathbf{x}} + G_{E,s,y}^{\text{dif}} \hat{\mathbf{y}} \otimes \hat{\mathbf{y}} + G_{E,s,z}^{\text{dif}} \hat{\mathbf{z}} \otimes \hat{\mathbf{z}}$$
$$\pm G_{E,s,\text{mix}}[\hat{\mathbf{x}} \otimes \hat{\mathbf{z}} - \hat{\mathbf{z}} \otimes \hat{\mathbf{x}}], \tag{B4}$$

with

$$G_{E,s,x/y}^{\text{dif}} = i \int_0^\infty \frac{dk_\perp k_\perp}{8\pi k_z} e^{2ik_z(d+R)} [r_s(J_0(k_\perp l) \pm J_2(k_\perp l))$$
$$- r_p \frac{k_z^2}{k_0^2}(J_0(k_\perp l) \mp J_2(k_\perp l))], \tag{B5}$$

as well as

$$G_{E,s,z}^{\text{dif}} = i \int_0^\infty \frac{dk_\perp k_\perp^3}{4\pi k_0^2 k_z} e^{2ik_z(d+R)} r_p J_0(k_\perp l), \tag{B6}$$

$$G_{E,s,\text{mix}} = \int_0^\infty \frac{dk_\perp k_\perp^2}{4\pi k_0^2} e^{2ik_z(d+R)} r_p J_1(k_\perp l), \tag{B7}$$

otherwise. For the correlation function of the background fields, we obtain

$$\mathbb{C}_{b,11/22} = \mathcal{C}_{b,\perp}^{\text{id}}(\hat{\mathbf{x}} \otimes \hat{\mathbf{x}} + \hat{\mathbf{y}} \otimes \hat{\mathbf{y}}) + \mathcal{C}_{b,z}^{\text{id}} \hat{\mathbf{z}} \otimes \hat{\mathbf{z}} \tag{B8}$$

with

$$C_{b,\perp}^{\text{id}} = \int_0^{k_0} \frac{dk_\perp k_\perp}{8\pi k_z} \left[R_s^+(k_\perp, d) + R_p^-(k_\perp, d) \frac{k_z^2}{k_0^2} \right], \tag{B9}$$

$$C_{b,z}^{\text{id}} = \int_0^{k_0} \frac{dk_\perp k_\perp^3}{4\pi k_z k_0^2} R_p^+(k_\perp, d), \tag{B10}$$

in the case of identical particles and

$$\mathbb{C}_{b,12/21} = \mathcal{C}_{b,x}^{\text{dif}} \hat{\mathbf{x}} \otimes \hat{\mathbf{x}} + \mathcal{C}_{b,y}^{12/21} \hat{\mathbf{y}} \otimes \hat{\mathbf{y}} + \mathcal{C}_{b,z}^{\text{dif}} \hat{\mathbf{z}} \otimes \hat{\mathbf{z}}$$
$$+ \mathcal{C}_{b,xz}^{12/21} \hat{\mathbf{x}} \otimes \hat{\mathbf{z}} + \mathcal{C}_{b,zx}^{12/21} \hat{\mathbf{z}} \otimes \hat{\mathbf{x}}, \tag{B11}$$

with

$$C_{b,x/y}^{\text{dif}} = \int_0^{k_0} \frac{dk_\perp k_\perp}{8\pi k_z} \left[R_s^+(k_\perp, d)[J_0(k_\perp l) \pm J_2(k_\perp l)] \right.$$
$$\left. + R_p^-(k_\perp, d) \frac{k_z^2}{k_0^2}[J_0(k_\perp l) \mp J_2(k_\perp l)] \right], \tag{B12}$$

$$C_{b,z}^{\text{dif}} = \int_0^{k_0} \frac{dk_\perp k_\perp^3}{4\pi k_z k_0^2} R_p^+(k_\perp, d) J_0(k_\perp l), \tag{B13}$$

as well as

$$C_{b,xz}^{12/21} = \pm i \int_0^{k_0} \frac{dk_\perp k_\perp^2}{4\pi k_0^2} \tilde{R}_p^-(k_\perp, d) J_1(k_\perp l), \tag{B14}$$

$$C_{b,zx}^{12/21} = \pm i \int_0^{k_0} \frac{dk_\perp k_\perp^2}{4\pi k_0^2} \tilde{R}_p^+(k_\perp, d) J_1(k_\perp l), \tag{B15}$$

if one considers different particles. Here we introduced

$$R_i^\pm(k_\perp, d) = 1 + |r_i|^2 \pm 2\text{Re}(e^{2ik_z(d+R)} r_i), \tag{B16}$$

$$\tilde{R}_i^\pm(k_\perp, d) = 1 - |r_i|^2 \pm 2i\text{Im}(2e^{ik_z(d+R)} r_i). \tag{B17}$$

In the same way we obtain for the correlation function of the substrate fields

$$\mathbb{C}_{s,11/22} = \mathcal{C}_{s,\perp}^{\text{id}}(\hat{\mathbf{x}} \otimes \hat{\mathbf{x}} + \hat{\mathbf{y}} \otimes \hat{\mathbf{y}}) + \mathcal{C}_{s,z}^{\text{id}} \hat{\mathbf{z}} \otimes \hat{\mathbf{z}}, \tag{B18}$$

with

$$C_{s,\perp}^{\text{id}} = \int_0^{k_0} \frac{dk_\perp k_\perp}{8\pi k_z}\left[1 - |r_s|^2 + \frac{k_z^2}{k_0^2}(1 - |r_p|^2)\right]$$
$$+ \int_{k_0}^{\infty} \frac{dk_\perp k_\perp}{4\pi |k_z|} e^{-2|k_z|(d+R)}\left[\text{Im}(r_s) + \frac{|k_z|^2}{k_0^2}\text{Im}(r_p)\right]$$

(B19)

and

$$C_{s,z}^{\text{id}} = \int_0^{k_0} \frac{dk_\perp k_\perp^3}{4\pi k_z k_0^2}(1 - |r_p|^2) + \int_{k_0}^{\infty} \frac{dk_\perp k_\perp^3}{2\pi |k_z| k_0^2} e^{-2|k_z|d}\text{Im}(r_p)$$

(B20)

for the case of two identical particles and

$$\mathbb{C}_{s,12/21} = \mathcal{C}_{s,x}^{\text{dif}}\hat{\mathbf{x}} \otimes \hat{\mathbf{x}} + \mathcal{C}_{s,y}^{\text{dif}}\hat{\mathbf{y}} \otimes \hat{\mathbf{y}} + \mathcal{C}_{s,z}^{\text{dif}}\hat{\mathbf{z}} \otimes \hat{\mathbf{z}}$$
$$+ \mathcal{C}_{s,xz}^{12/21}\hat{\mathbf{x}} \otimes \hat{\mathbf{z}} + \mathcal{C}_{s,zx}^{12/21}\hat{\mathbf{z}} \otimes \hat{\mathbf{x}},$$

(B21)

with

$$C_{s,x/y}^{\text{dif}} = \int_0^{k_0} \frac{dk_\perp k_\perp}{8\pi k_z}[\Gamma_+ J_0(k_\perp l) \pm \Gamma_- J_2(k_\perp l)]$$
$$+ \int_{k_0}^{\infty} \frac{dk_\perp k_\perp}{4\pi |k_z|} e^{-2|k_z|(d+R)}[\Delta_+ J_0(k_\perp l) \pm \Delta_- J_2(k_\perp l)]$$

(B22)

$$C_{s,z}^{\text{dif}} = \int_0^{k_0} \frac{dk_\perp k_\perp^3}{4\pi k_z k_0^2}(1 - |r_p|^2)J_0(k_\perp l)$$
$$+ \int_{k_0}^{\infty} \frac{dk_\perp k_\perp^3}{2\pi |k_z| k_0^2} e^{-2|k_z|(d+R)}\text{Im}(r_p)J_0(k_\perp l),$$

(B23)

and

$$C_{s,xz}^{12/21} = \mp i\int_0^{k_0} \frac{dk_\perp k_\perp^2}{4\pi k_0^2}(1 - |r_p|^2)J_1(k_\perp l)$$
$$\pm \int_{k_0}^{\infty} \frac{dk_\perp k_\perp^2}{2\pi k_0^2} e^{-2|k_z|(d+R)}\text{Im}(r_p)J_1(k_\perp l),$$

(B24)

$$C_{s,zx}^{12/21} = \mp i\int_0^{k_0} \frac{dk_\perp k_\perp^2}{4\pi k_0^2}(1 - |r_p|^2)J_1(k_\perp l)$$
$$\mp \int_{k_0}^{\infty} \frac{dk_\perp k_\perp^2}{2\pi k_0^2} e^{-2|k_z|(d+R)}\text{Im}(r_p)J_1(k_\perp l),$$

(B25)

in the case of two different particles. Here we introduced

$$\Gamma_\pm = 1 - |r_s|^2 \pm \frac{k_z^2}{k_0^2}(1 - |r_p|^2),$$

(B26)

$$\Delta_\pm = \text{Im}(r_s) \pm \frac{|k_z|^2}{k_0^2}\text{Im}(r_p).$$

(B27)

---

[1] W. Srituravanich, N. Fang, C. Sun, Q. Luo, and X. Zhang, Plasmonic nanolithography, Nano Lett. **4**, 1085 (2004).

[2] W. A. Challener, C. Peng, A. V. Itagi, D. Karns, W. Peng, Y. Peng, X. M. Yang, X. Zhu, N. J. Gokemeijer, Y.-T. Hsia, G. Ju, R. E. Rottmayer, M. A. Seigler, and E. C. Gage, Heat-assisted magnetic recording by a near-field transducer with efficient optical energy transfer, Nat. Photon. **3**, 220 (2009).

[3] B. C. Stipe, T. C. Strand, C. C. Poon, H. Balamane, T. D. Boone, J. A. Katine, J.-L. Li, V. Rawat, H. Nemoto, A. Hirotsune, O. Hellwig, R. Ruiz, E. Dobisz, D. S. Kercher, N. Robertson, T. R. Albrecht, and B. D. Terris, Magnetic recording at 1.5 pb m⁻² using an integrated plasmonic antenna, Nat. Photon. **4**, 484 (2010).

[4] K. Kim, B. Song, V. Fernandez-Hurtado, W. Lee, W. Jeong, L. Cui, D. Thompson, J. Feist, M. T. H. Reid, F. J. Garcia-Vidal, J. C. Cuevas, E. Meyhofer, and P. Reddy, Radiative heat transfer in the extreme near field, Nature (London) **528**, 387 (2015).

[5] A. Kittel, U. Wischnath, J. Welker, O. Huth, F. Rüting, and S.-A. Biehs, Near-field thermal imaging of nanostructured surfaces, Appl. Phys. Lett. **93**, 193109 (2008).

[6] Y. de Wilde, F. Formanek, R. Carminati, B. Gralak, P.-A. Lemoine, K. Joulain, J.-P. Mulet, Y. Chen, and J.-J. Greffet, Thermal radiation scanning tunnelling microscopy, Nature (London) **444**, 740 (2006).

[7] A. C. Jones and M. B. Raschke, Thermal infrared near-field spectroscopy, Nano Lett. **12**, 1475 (2012).

[8] Y. Kajihara, K. Kosaka, and S. Komiyama, A sensitive near-field microscope for thermal radbiation, Rev. Sci. Instrum. **81**, 033706 (2010).

[9] M. Planck, *The Theory of Heat Radiation* (P. Blakiston's Son & Co., Philadelphia, 1914).

[10] D. Polder and M. van Hove, Theory of radiative heat transfer between closely spaced bodies, Phys. Rev. B **4**, 3303 (1971).

[11] A. I. Volokitin and B. N. J. Persson, Near-field radiative heat transfer and noncontact friction, Rev. Mod. Phys. **79**, 1291 (2007).

[12] K. Joulain, J.-P. Mulet, F. Marquier, R. Carminati, and J.-J. Greffet, Surface electromagnetic waves thermally excited: Radiative heat transfer, coherence properties and Casimir forces revisited in the near field, Surf. Sci. Rep. **57**, 59 (2005).

[13] K. L. Nguyen, O. Merchiers, and P.-O. Chapuis, Near-field radiative heat transfer in scanning thermal microscopy computed with the boundary element method, J. Quant. Spectrosc. Radiat. Transf. **202**, 154 (2017).

[14] A. Narayanaswamy, S. Shen, and G. Chen, Near-field radiative heat transfer between a sphere and a substrate, Phys. Rev. B **78**, 115303 (2008).

[15] A. P. McCauley, M. T. H. Reid, M. Krüger, and S. G. Johnson, Modeling near-field radiative heat transfer from sharp objects using a general three-dimensional numerical scattering technique, Phys. Rev. B **85**, 165104 (2012).

[16] S. Edalatpour and M. Francoeur, Near-field radiative heat transfer between arbitrarily shaped objects and a surface, Phys. Rev. B **94**, 045406 (2016).

[17] F. Herz, Z. An, S. Komiyama, and S.-A. Biehs, Revisiting the dipole model for a thermal infrared near-field spectroscope, Phys. Rev. Appl. **10**, 044051 (2018).

[18] F. Herz and S.-A. Biehs, Generalized coupled dipole method for thermal far-field radiation, Phys. Rev. B **105**, 205422 (2022).

[19] P. Ben-Abdallah, Multitip near-field scanning thermal microscopy, Phys. Rev. Lett. **123**, 264301 (2019).

[20] P. Ben-Abdallah, S.-A. Biehs, and K. Joulain, Many-body radiative heat transfer theory, Phys. Rev. Lett. **107**, 114301 (2011).

[21] R. Messina, M. Tschikin, S.-A. Biehs, and P. Ben-Abdallah, Fluctuation-electrodynamic theory and dynamics of heat transfer in systems of multiple dipoles, Phys. Rev. B **88**, 104307 (2013).

[22] S.-A. Biehs, R. Messina, P. S. Venkataram, A. W. Rodriguez, J. C. Cuevas, and P. Ben-Abdallah, Near-field radiative heat transfer in many-body systems, Rev. Mod. Phys. **93**, 025009 (2021).

[23] S. M. Rytov, Y. A. Kravtsov, and V. I. Tatarskii, *Principles of Statistical Radiophysics: Elements of Random Fields* (Springer, Berlin, 1989), Vol. 3.

[24] B. T. Draine, The discrete-dipole approximation and its application to interstellar graphite grains, Astrophys. J. **333**, 848 (1988).

[25] C. Otey and S. Fan, Numerically exact calculation of electromagnetic heat transfer between a dielectric sphere and plate, Phys. Rev. B **84**, 245431 (2011).

[26] A. Narayanaswamy and G. Chen, Thermal near-field radiative transfer between two spheres, Phys. Rev. B **77**, 075125 (2008).

[27] P. Ben-Abdallah, K. Joulain, J. Drevillon, and C. Le Goff, Heat transport through plasmonic interactions in closely spaced metallic nanoparticle chains, Phys. Rev. B **77**, 075417 (2008).

[28] S. Edalatpour, M. Čuma, T. Trueax, R. Backman, and M. Francoeur, Convergence analysis of the thermal discrete dipole approximation, Phys. Rev. E **91**, 063307 (2015).

[29] C. A. Brebbia, J. Telles, and L. Wrobel, *Boundary Elements Techniques: Theory and Applications in Engineering* (Springer Verlag, Berlin, 1984).

[30] J. Dong, J. Zhao, and L. Liu, Radiative heat transfer in many-body systems: Coupled electric and magnetic dipole approach, Phys. Rev. B **95**, 125411 (2017).

[31] P. M. Tomchuk and N. I. Grigorchuk, Shape and size effects on the energy absorption by small metallic particles, Phys. Rev. B **73**, 155423 (2006).

[32] G. V. Dedkov and A. A. Kyasov, Thermal radiation of nanoparticles occurring at a heated flat surface in vacuum, Tech. Phys. Lett. **33**, 305 (2007).

[33] P.-O. Chapuis, M. Laroche, S. Volz, and J.-J. Greffet, Radiative heat transfer between metallic nanoparticles, Appl. Phys. Lett. **92**, 201906 (2008).

[34] P.-O. Chapuis, M. Laroche, S. Volz, and J.-J. Greffet, Near-field induction heating of metallic nanoparticles due to infrared magnetic dipole contribution, Phys. Rev. B **77**, 125402 (2008).

[35] R. M. Abraham Ekeroth, A. García-Martín, and J. C. Cuevas, Thermal discrete dipole approximation for the description of thermal emission and radiative heat transfer of magneto-optical systems, Phys. Rev. B **95**, 235428 (2017).

[36] A. Lakhtakia, Strong and weak forms of the method of moments and the coupled dipole method for scattering of time-harmonic electromagnetic fields, Int. J. Mod. Phys. C **03**, 583 (1992).

[37] S. Albaladejo, R. Gómez-Medina, L. S. Froufe-Pérez, H. Marinchio, R. Carminati, J. F. Torrado, G. Armelles, A. García-Martín, and J. J. Sáenz, Radiative corrections to the polarizability tensor of an electrically small anisotropic dielectric particle, Opt. Expr. **18**, 3556 (2010).

[38] R. Carminati, J.-J. Greffet, C. Henkel, and J. M. Vigoureux, Radiative and non-radiative decay of a single molecule close to a metallic nanoparticle, Opt. Commun. **261**, 368 (2006).

[39] E. W. Palik, *Handbook of Optical Constants of Solids* (Academic Press, San Diego, CA, 1985).

[40] W. Eckhardt, Macroscopic theory of electromagnetic fluctuations and stationary radiative heat transfer, Phys. Rev. A **29**, 1991 (1984).

[41] R. Messina and M. Antezza, Scattering-matrix approach to Casimir-Lifshitz force and heat transfer out of thermal equilibrium between arbitrary bodies, Phys. Rev. A **84**, 042102 (2011).

[42] F. Herz and S.-A. Biehs, Thermal radiation and near-field thermal imaging of a plasmonic Su-Schrieffer-Heeger chain, Appl. Phys. Lett. **121**, 181701 (2022).

[43] C. A. Downing, E. Mariani, and G. Weick, Retardation effects on the dispersion and propagation of plasmons in metallic nanoparticle chains, J. Phys.: Condens. Matter **30**, 025301 (2018).

[44] See Supplemental Material at http://link.aps.org/supplemental/10.1103/PhysRevB.110.125410 for three videos containing the power distribution for the remaining 10 layouts—one for each distance.

[45] D. Cao, A. Cazé, M. Calabrese, R. Pierrat, N. Bardou, S. Collin, R. Carminati, V. Krachmalnicoff, and Y. de Wilde, Mapping the radiative and the apparent nonradiative local density of states in the near field of a metallic nanoantenna, ACS Photon. **2**, 189 (2015).

[46] D. Bouchet, J. Scholler, G. Blanquer, Y. de Wilde, I. Izeddin, and V. Krachmalnicoff, Probing near-field light-matter interactions with single-molecule lifetime imaging, Optica **6**, 135 (2019).

[47] U. Hohenester, H. Ditlbacher, and J. R. Krenn, Electron-energy-loss spectra of plasmonic nanoparticles, Phys. Rev. Lett. **103**, 106801 (2009).

[48] P. Lodahl, A. F. van Driel, I. S. Nikolaev, A. Irman, K. Overgaag, D. Vanmaekelbergh, and W. L. Los, Controlling the dynamics of spontaneous emission from quantum dots by photonic crystals, Nature (London) **430**, 654 (2004).

[49] M. D. Birowosuto, S. E. Skipetrov, W. L. Vos, and A. P. Mosk, Observation of spatial fluctuations of the local density of states in random photonic media, Phys. Rev. Lett. **105**, 013904 (2010).

[50] J. E. Sipe, New Green-function formalism for surface optics, J. Opt. Soc. Am. B **4**, 481 (1987).